Space Science Reviews (2026) 222:31
https://doi.org/10.1007/s11214-026-01288-5

The Asteroid Framing Cameras on ESA's Hera Mission

Jean-Baptiste Vincent[1] · Gábor Kovács[2] · Balázs V. Nagy[2] · Frank Preusker[1] · Naomi Murdoch[3] · Maurizio Pajola[4] · Michael Kueppers[5] · Patrick Michel[6,7] · Seiji Sugita[7] · Hannah Goldberg[8]

Received: 6 November 2024 / Accepted: 5 March 2026

Abstract
As the first asteroid deflection test, NASA's successfully hit asteroid Dimorphos (secondary of the binary asteroid 65803 Didymos) with the DART kinetic impactor on September 26, 2022. To fully characterise the physical properties of the objects, and measure precisely the effects of this impact in the context of planetary defence, ESA launched the Hera mission on 7 October 2024, with scheduled arrival at Didymos in fall 2026. Among the core payload of the mission, the Asteroid Framing Cameras are two identical imaging systems that will support navigation and scientific activities, by acquiring images from various distances and observing geometries during the course of the mission. Built by Jena-Optronik (Germany), the cameras match the requirements designed by the science team and will provide data that supports a wide range of investigations: hazard detection, system dynamics, shape reconstruction, surface morphology and mapping, and surface photometry. Each instrument is a panchromatic camera equipped with a 5.5 × 5.5 degree field of view, and an angular resolution of 93.7 micro-radians per pixel. The cameras shall provide the necessary data to address the mission requirements through a global mapping of the two components of the binary system at spatial scales of 2–3 m/pixel in the Early Characterisation Phase, 1–2 m/pixel in the Detailed Characterisation Phase, and 0.5–2 m/pixel in the Close Operation Phase. Dedicated flybys will bring the resolution down to < 10 cm/pixel on specific areas of interest on Dimorphos, such as the DART impact site and the JUVENTAS cubesat landing site. Here, we present the technical specifications of the camera, as well as the status of the calibration. We then summarise the planned operations in cruise and at the asteroids. Finally, we provide examples of the scientific investigations and products that will make use of the data returned by the cameras.

Keywords Remote sensing · Camera · Asteroid · Hera · Didymos

1 Introduction

Hera is the European Space Agency (ESA) component of the large international project AIDA: Asteroid Impact and Deflection Assessment. The mission is designed to study the effects of a kinetic impact on an asteroid in the context of international Planetary Defence activities (Michel et al. 2022). More specifically, Hera will assess the outcome of NASA's Double Asteroid Redirection Test (DART, Cheng et al. 2018) which intentionally collided with

Extended author information available on the last page of the article

the small moon called Dimorphos of the binary asteroid (65803) Didymos on 26 September 2022. DART achieved its objective of hitting the target asteroid at more than 6 km/s (Daly et al. 2023), and created a measurable decrease of its orbital period around the larger parent asteroid Didymos (Thomas et al. 2023). However, a true assessment of the efficiency of the deflection, necessary for designing future responses to actual hazardous asteroids, requires a dedicated mission for in-depth characterisation. That is exactly the purpose of Hera. After launch on 7 October 2024, Hera will reach the Didymos system in late 2026 with the following goals:

- determine dynamical properties of the Didymos system: semi-major axis, eccentricity, spin rates and orientation
- measure global physical properties of each asteroid; including internal ones: mass, volume, density, size distribution of surface material
- characterise the shape of the DART crater, and/or extent of large scale reshaping
- assess the presence of excavated material on the surface or in the system and determine its size distribution

These primary objectives are necessary to fully establish the momentum transfer imparted by DART (a preliminary assessment can be found in Cheng et al. 2023), and thus close the AIDA experiment. A more detailed description of the mission, including all requirements and a science traceability matrix can be found in Michel et al. (2022).

To achieve these goals, Hera carries a selection of payload carefully chosen to meet the primary requirements of the mission. In this article, we focus on the Asteroid Framing Cameras, a set of two identical panchromatic imaging instruments to be used as the core payload for navigation and asteroid characterisation. In the following sections, we will introduce the instruments and their technical specifications, the high-level operational plan for the mission, and the calibration measurements that have been acquired before launch. We will conclude with an overview of the expected scientific return to be enabled by the AFCs, which extends beyond the Planetary Defence requirements of the mission, due to the unique nature of the Didymos system and the many open questions brought forward by DART (e.g. see morphological considerations in Barnouin et al. (2024)

2 Requirements and Specifications

The Asteroid Framing Cameras (AFC) are a core payload of Hera, necessary for both navigation and completion of the mission objectives. As a risk mitigation measure, the mission flys with two identical cameras, AFC1 and AFC2, which have the exact same specifications and performance. Both cameras are totally interchangeable for all intents and purposes. During the mission, all calibration operations are implemented and executed identically for both instruments. However, Science/Navigation data is acquired exclusively with AFC1, and AFC2 is reserved for contingency mitigation.

The AFC are panchromatic cameras with refractive optics, operating in the visible wavelength range (400-900 nm). Provided by Jena-Optronik, they are based on the ASTROhead design,[1] and use a FaintStar2 CMOS detector.[2] A detailed list of the cameras specifications is provide in Table 1. These cameras have the highest Technology Readiness Level (TRL9),

[1] https://www.jena-optronik.de/products/cameras-and-camera-systems/astrohead-cam.html, retrieved on 2025-11-03.

[2] https://caeleste.be/news/eyes-on-hera-with-faintstar2-detector-chip/, retrieved on 2025-11-03.

Table 1 Specifications (from manufacturer)

Parameter	Value
Field of View	$5.5 \times 5.5°$
Image size	1020×1020 pixel
Focal length	105.57 mm
F-number	4.2
Angular scale	94.1 μrad/px
Spectral range	400-900 nm
A/D resolution	12 bits (4096 values)
ADC conversion	32 e^-/DN
Integration time	224 μs to 5 s
Readout frequency	Up to 4 Hz
Data volume / image	1.5 MByte
Mass	1.1 kg
Power	0.9 W

having successfully flown on multiple missions. The first ASTROhead Cam flight set was used on Northrop Grumman's Mission Extension Vehicle MEV-1 in 2019, which made a rendez-vous with commercial satellite Intelsat 901 on 25 February 2020. A similar mission MEV-2, docked with Intelsat 10-02 on a geostationary orbit on 12 April 2021, once again supported by a set of ASTROhead cameras.

Besides the high TRL, the AFC were selected because they fulfill all mission requirements for an imaging instrument. The most relevant constraints are the following (from ESA's Hera Mission Requirements document):[3]

1. Hera shall identify the DART impact area on Dimorphos and acquire data to reconstruct the tri-dimensional shape of the eventual crater to an accuracy of 50 cm. Because of the inherent loss of resolution from 3D reconstruction techniques, this requires an image pixel scale of 10 cm (one needs to correlate multiple images of the same region with varying viewing geometry and the matching of features between image pairs require multiple pixels). For safety, Hera remains outside of the orbit of Dimorphos and does not approach closer than 1 km from either asteroid during the nominal mission. At this distance, the 10 cm/px requirement constrains the angular scale (a.k.a. IFoV: Instantaneous Field-of-View) to be 100 μrad/px or smaller.
2. Hera shall determine the mass of Dimorphos within 10%. This can be achieved by determining the motion of Didymos around the common centre of mass of Didymos and Dimorphos to an accuracy of 1 m, by tracking landmarks on the surface of the asteroids. To guarantee a successful tracking, it is preferable that the camera can observe the full body of Didymos during several orbits of Dimorphos, with a pixel scale of 1 meter. The previous requirement already constrains the angular resolution; from which we know that a pixel scale of 1 m can be obtained from a distance of 10 km. At this distance, the angular size of Didymos (max diameter 850 m) is 4.85°, which sets the minimum size of the camera field-of-view.

Therefore, the minimum set of constraints for an imaging instrument on Hera are IFOV $<= 100$ μrad/px and FOV $>= 4.85°$. Table 1 shows that the AFC surpasses both requirements.

[3] https://www.heramission.space/missionrequirementsdocuments, retrieved on 2025-11-03.

3 Calibration

The AFC is a space certified instrument designed for navigation. For scientific use, one needs to ensure a thorough calibration on-ground and in-flight, in order to convert reliably the pixel values (Digital Numbers, a.k.a. DN) into physical quantities (e.g. asteroid reflectance). Here we describe the methods and results of the Hera AFC ground calibration. The optical tests and the image acquisitions have been performed in December 2022 and January 2023, at Jena Optronik (JOP) in Jena, Germany. All tasks were based on recommendations from the Hera Investigation Team, and follow procedures developed for imaging instruments on previous missions (i.e. Kovács et al. 2024). The analysis and the evaluation of the results have been performed at the Budapest University of Technology and Economics, Department of Mechatronics, Optics and Engineering Informatics. The procedure and results have been evaluated and validated by the Hera Investigation Team, within the frame work of the "Hera Data Analysis, Exploitation, Interpretation Working Group" (a.k.a. WG4).

The calibration tests were carried out with the same settings as currently planned for the scientific imaging phases of the mission:

- Full field of view (1020x1020 pixels)
- 12 bits ADC setting, providing 4096 DN levels for each image
- No image compression was used
- Commanded exposure time was set between 0.224 ms and 5000.0 ms, covering the full range of capabilities of the instrument
- The acquired images were stored as standard FITS image files. The FITS header contains the camera settings, exposure time, temperatures, and other information about the instruments and the actual operation.

In the following subsections, we detail the calibration methods and results related to on-ground measurement of dark, bias, flat fields, linearity, and optical distortion.

3.1 Dark & Bias

The temperature dependency dark test has been carried out by the JOP personnel in December 2022, in a thermal vacuum chamber at the JOP optical laboratory. The tests resulted in FITS data cubes at various temperatures and exposure times. The nominal (interface plate) temperatures were set to -25 °C, -15 °C, 0 °C, 10 °C, 20 °C, 35 °C and 45 °C. The actual detector temperatures are sometimes slightly higher due to the interface plate in the setup, but the actual sensor temperature was recorded and stored in the FITS header. After stabilising the system at each temperature, image cubes were acquired with 0.224 ms, 100 ms, 500 ms, 1000 ms, and 5000 ms exposure times. Each cube consists of 30 images acquired with the same exposure and detector temperature. During the tests, the camera aperture was covered by a black cup, and the laboratory lights were switched off. The ambient temperature was also recorded.

The camera does not have a shutter, therefore a true 0 ms exposure is not possible. For this reason, the bias frame is approximated by the shortest possible dark exposure time, which was 0.224 ms. The maximum dark exposure time was 5000 ms.

General findings:

- The bias images showed the expected uniform noise pattern in the ± 2 DNs range.
- The individual bias images did not exhibit any structure or pattern noise, only random noise was visible.
- The average bias value was stable throughout the full test campaign within ± 1 DN.

- The bias images exhibited a slight temperature dependency in the fraction of a DN (it might be the effect of the finite exposure time).
- The short exposure dark images showed the expected uniform noise pattern.
- The exposure time increase resulted in the expected linear DN increase.
- The 1000 ms and 5000 ms dark images exhibited a slight increase in the background values towards the detector edges, which might be an effect of a chip temperature gradient. The average increase was 11 DNs at 35 °C interface temperature, and 5000 ms exposure.

For each camera, a master bias frame for the calibration pipeline was created from the 20 °C interface temperature image cube. The FITS cube contains 30 consecutive images with 0.224 ms exposure time. Each pixel of the reference bias frame is calculated as the median of the same coordinate 30 pixels. This median bias image is stored as a single frame FITS image for each camera as: "AFC1_BIAS_V1.0.FTS" and "AFC2_BIAS_V1.0.FTS" and used for the calculations in the data processing of all calibration measurements.

Similarly, master dark frames for the calibration pipeline were created from the 20 °C interface temperature image cube. The FITS cube contains 30 consecutive images with 999.904 ms exposure time. Each pixel of the reference dark frame is calculated as the median of the same coordinate 30 pixels. This median dark image is stored as a single frame FITS image for each camera as: "AFC1_DARK_V1.0.FTS" and "AFC2_DARK_V1.0.FTS" and used for the calculations in the data processing of all calibration measurements. The actual detector temperature of the master dark frame is recorded in the image header and should be used during the scaling of the dark frame.

The dark current D (in DN/s) of a typical pixel follows the formula:

$$D(T) = Ae^{\frac{-B}{k_B T}}$$

where $A = 8.91 \times 10^{12}$, $B = 1.02 \times 10^{-19}$ are instrument-specific constants, T is the detector temperature in Kelvin, and k_B is Boltzmann's constant (1.38×10^{-23} $\mathrm{m^2 kgs^{-2} K^{-1}}$).

In practical terms, the change of temperature needed to double the dark current is given by:

$$\frac{1}{T_2} = \frac{1}{T_1} - \frac{k_B \ln 2}{B}$$

with temperatures expressed in Kelvin.

For the reference temperature $T_1 = 20.0\ ^\circ C$ (293.15 K), we get $T_2 = 28.28\ ^\circ C$ (301.28 K), i.e. an increase of 8.13 $^\circ C$.

The scaling factor for the reference dark frame is given by:

$$C_{\mathrm{dark}} = \frac{t_{\mathrm{exp}}}{t_{\mathrm{expDark}}} e^{\left(\frac{-B}{k_B}\left(\frac{1}{T_{\mathrm{CMOS}}} - \frac{1}{T_{\mathrm{dark}}}\right)\right)}$$

where t_{exp} is the exposure time of the actual frame, t_{expDark} the exposure time of the dark frame, T_{CMOS} is the detector temperature of the actual frame, T_{dark} the exposure temperature of the dark frame.

Images acquired in the thermal-vacuum chamber (TVAC) with the shortest exposure were examined for bad pixels. A median image was calculated from each temperature cubes. No dead pixels were detected, but there are 7 "hot pixels", with DN values above the median (3 for AFC1, 4 for AFC2). These pixels are listed in Table 2 and will be monitored during the mission. Pixels with 20 DNs larger than the frame average (approx. 17 DN) are considered suspicious.

Table 2 Image coordinates (row, column) of hot pixels. (0,0) is the top left corner in the FITS files

AFC1 row, column	AFC2 row, column
322, 490	923, 101
645, 516	912, 152
463, 775	828, 254
	688, 866

3.2 Flat Field Tests

The flat field tests utilised a 0.5 m diameter integrating sphere. The camera was mounted horizontally, with the optical axis facing the entrance aperture of the integrating sphere. The sphere was moved close to the camera baffle to avoid vignetting by the entrance aperture. The sphere's back surface was illuminated by halogen light sources, covering the full wavelength range of the AFC camera. The lamps' current was gradually increased to 1.600 A. After 10 minutes, the lamps stabilised, and the flat images were acquired. Three image cubes have been recorded with ten frames in each data file. The exposure times were set to 0.224 ms, 0.436 ms and 0.648 ms. This corresponds to approximately 25%, 50%, and 75% maximum intensity in the central image regions.

The images show a uniformly illuminated field of view, with a slight (4-6%) drop in intensity towards the edges. The frames do not show signs of dust or other contamination of the detector or the optical components. The two cameras have very similar flat images, and no sign of disturbing stray-light effects, vignetting, or internal reflections.

The normalised flat images are separated into a low-frequency component by applying a 200 px Gaussian blur on it, and a high-frequency component by subtracting the low-frequency component. The normalised standard deviation of the high-frequency components is less than 0.005. The normalised standard deviation of the low-frequency components is less than 0.015.

The master flat frame for the calibration pipeline was created from the 0.436 ms exposure flat cubes, with the applied processing steps:

- The median image was calculated from the 10 cube frames.
- The median was converted to a 64-bit PC double image.
- The master bias image was subtracted from the median.
- The image was normalised (scaled) to have the central 200×200 pixels average a value of 1.0.

Figure 1 shows the reference master flats for AFC1 and AFC2.

3.3 Linearity

The linearity test utilised the same optical setup as the flat field test. The camera was mounted horizontally, with the optical axis facing the entrance aperture of the 0.5 m integrating sphere. The sphere was moved close to the camera baffle to avoid vignetting. The sphere back surface was illuminated by halogen light sources, covering the full wavelength range of the AFC camera. The nominal sphere illumination was too high for the sensitivity of the camera and allowed only four exposure steps without saturation. For this reason, the sphere illumination was decreased by adjusting a lower lamp current than for the flat test. After switching on, the current of the lamps was gradually increased to 1.150 A. After

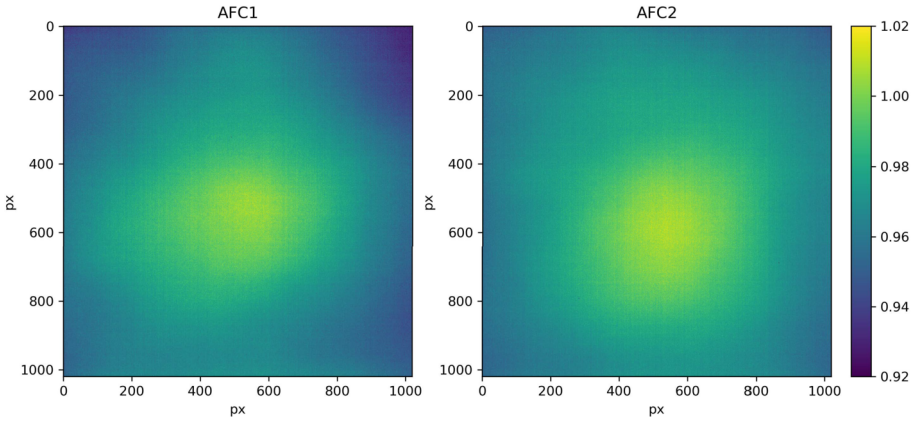

Fig. 1 Master Flat images for AFC1 (left) and AFC2 (right)

10 minutes, the lamps stabilised, and the linearity images were acquired. A total of 28 image cubes have been recorded, with three frames in each data file. The exposure time was gradually increased from 0.224 ms to 5.951 ms.

For each data cube (with the same exposure settings) we applied the following steps:

- The average image was calculated from the 3 cube frames.
- The master bias image was subtracted from the median.
- The image average pixel and standard deviation were calculated.
- A linear fit was calculated from the averages and the exposure times and used as an estimate of the ideal pixel averages.
- The linearity error was calculated as the difference between the actual and the ideal average.

This procedure checked the detector response linearity vs. exposure time, in the short exposure time regime. This exposure range will be used for most of the asteroid imaging (when the illuminated detector area is larger than a pixel size). The test exhibited relatively large errors for the very short exposures, and the linearity improved above the 1.0 ms exposure. For long exposure imaging (> 200 ms), the specific characteristics of the APS detectors must be considered: in the case of several hundred milliseconds exposure, the full well capacity of the pixels is significantly reduced. For instance, 800 ms exposure images would saturate around 3300 DNs, and longer exposure might further decrease the saturation level. This needs special attention at a low light level long exposure commanding since the detector is no longer saturated by the ADC (at 4096 DNs), but by the detector full well, at a lower DN value. Essentially, at short exposure times, the ADC saturates before the detector reaches full-well. However, as the exposure time increases, the detector reaches full-well or saturates before the ADC saturates and the level at which the device saturates drops with increasing exposure time.

We note that this behaviour, although undesirable, has no consequence on the instrument fulfillment of the mission requirements. All asteroid images will be acquired at very short exposure (typically < 10 ms), an order of magnitude less than the exposure threshold at which the image saturation level starts to decrease.

Figure 2 shows the results of the linearity measurements.

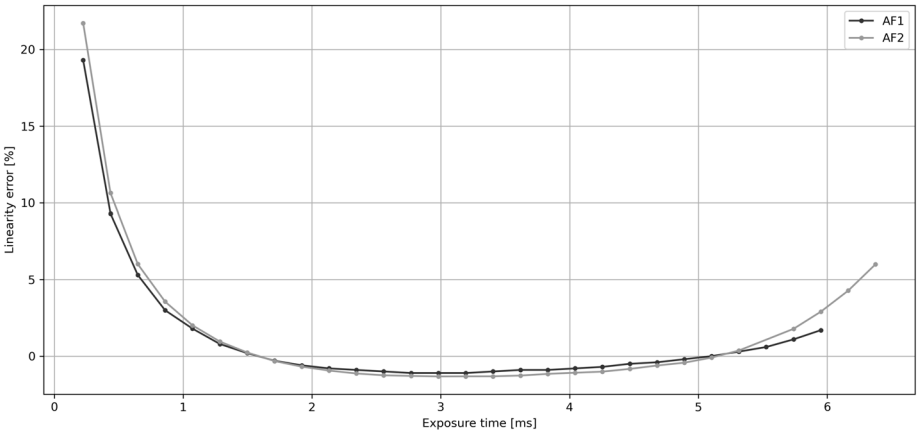

Fig. 2 Linearity error vs. exposure time at high intensities for both cameras

3.4 Residual Image Tests

The goal of the residual image test is to confirm the effectiveness of the detector clear process, and to check for the existence of a residual image from the previous exposure. Since the detector does not provide a true 0.0 ms exposure possibility (image readout without actual integration), the accurate determination of the residual image is difficult. The test utilised the same optical setup as the flat field test. The camera was mounted horizontally, with the optical axis facing the entrance aperture of the 0.5 m integrating sphere. The sphere was moved close to the camera baffle to avoid vignetting. The sphere's back surface was illuminated by halogen light sources, covering the full wavelength range of the AFC. The test commanded short exposure (0.224 ms) and long exposure (5.525 ms) image acquisition in a quick sequence, without wait time between them. The test was repeated four times.

After exposure, the bias removed images were visually examined for inconsistency and traces of residual DNs on the short exposure image. The ratio of the bias removed short and long exposure DN average was calculated.

The short exposure images did not show traces of residual image for any of the cameras, the average DNs correspond to the scaled long exposure image.

3.5 Radiometric Response

The radiometric test measured the camera response for a variable, narrow-band (quasi-monochromatic) light source. The source comprised a strong halogen light source, a grating monochromator, and a small integrating sphere. The monochromator scanned through the visible and NIR spectrum from 400 to 1000 nm, with 10 nm steps. The monochromator bandwidth was set to 10 nm. The monochromator output was coupled into a small integrating sphere. The camera was imaging the uniform radiation of the integrating sphere output aperture (10 mm diameter). Since the calibration target was not in focus, the image processing required integrating the flux in the ROI area. The actual output flux was monitored by a custom radiometer with calibrated Si diode.

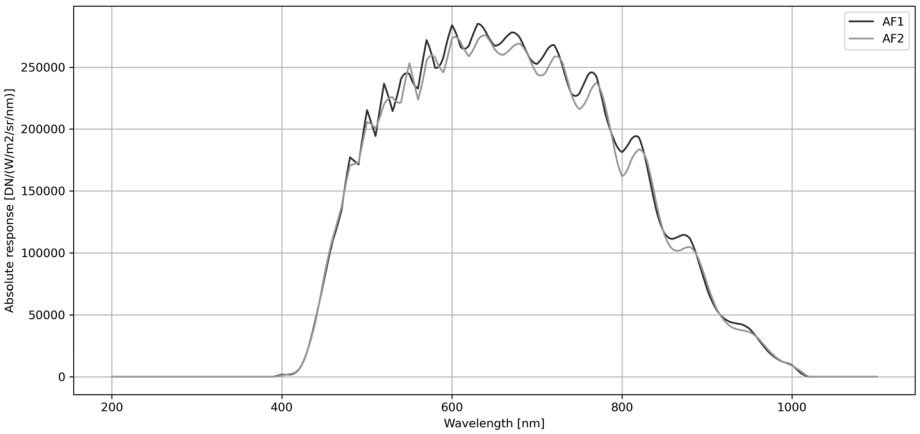

Fig. 3 Absolute response of the cameras as a function of wavelength

To process the image cubes, the following steps were carried out:

- The median of each image cube was calculated.
- The bias and dark were removed based on the master bias and the scaled master dark frame.
- Pixels on the "bad pixel list" are discarded.
- The camera response was calculated by aperture photometry. A circular aperture of 126 pixels in diameter was used to collect the monochromator flux, and a 50-pixel wide ring with a 0-pixel shift was used as the annulus.
- The output of the monochromator was monitored by a silicon diode, and its photo-current was converted to radiance units.

The two cameras provide a very similar radiometric response. The spectral characteristics match within 2% (Fig. 3). The integral camera responses are higher than the theoretical calculations based on the detector and optical data. This might indicate a slightly higher electronic gain value than specified. The spectral characteristics are also slightly different than expected from the detector specifications: Both cameras exhibit an oscillation of the response in the wavelength domain across the sensitive range. This might be the effect of some dichroic layers on the detector (or optics). Since the camera is acquiring only broadband monochromatic images, this does not create a significant problem; however, it decreases the photometric accuracy, especially for Solar illuminated targets.

In addition to the monochromatic tests, the camera radiometric response was also evaluated in the context of broad band imaging of an extended source, which is the actual mode relevant for all operations in the Didymos system. The test setup used a target lamp which had a circular aperture with Lambertian radiating surface. The radiance was calibrated in a certified calibration laboratory in Hungary.

The lamp was positioned at 4035 mm in front of the camera. The objects around the lamp and in the field of view of the camera were covered by black shading, to avoid stray light reflections. The lamp current was gradually increased to the nominal value. After the lamp stabilised, image cubes were acquired with correctly and overexposed settings. The overexposed images were intended to reveal possible stray light.

This setup is a good proxy for the asteroid approach phase when the target size is about 20% of the full field.

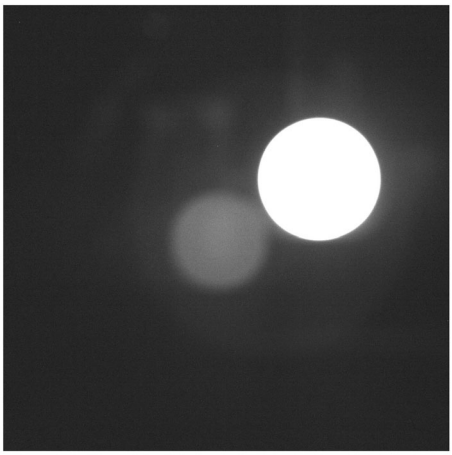

Fig. 4 Ghost pattern on the overexposed broad band image

Table 3 Radiometric calibration factors

Parameter	Value	Unit
AFC1 effective wavelength	654.7	nm
AFC1 effective FWHM	366.0	nm
AFC2 effective wavelength	655.6	nm
AFC2 effective FWHM	370.8	nm
General reference wavelength	650.0	nm
Solar Irradiance (1 AU)	1.5794	$W.m^{-2}.nm^{-1}$
Calib. Factor AFC1	9.5877×10^5	$DN.m^2.nm.W^{-1}.s^{-1}$
Calib. Factor AFC2	9.3698×10^5	$DN.m^2.nm.W^{-1}.s^{-1}$

FWHM: Full Width, Half Maximum

After exposure:

- The median of the image cube was calculated.
- The bias and dark were removed based on the master bias and the scaled master dark frame.
- The mean DN value of the central 51 pixels diameter area was calculated.
- The measured camera response was compared to the estimated values, based on the lamp radiance calibration.

We report that the expected radiance values match the lamp calibration measurements within 5%.

The broad band calibration lamp test also provided an opportunity to test for the presence of in-field stray light effects. When the lamp was not on the centre position, a slight ghost pattern was visible on all images in case of stretched intensity. The lamp position was also shifted by 150 mm, and overexposed images were also acquired. The intensity of the ghost pattern was very weak, less around 0.1% of the lamp image pattern (Fig. 4).

As a general recommendation, we calculated the camera reference wavelength from the camera DN response curves and the solar reference illumination, and measured the corresponding calibration factors. Recommended parameters are given in Table 3.

3.6 Geometric Distortion

The main objective of the test is to measure the camera geometric distortion, and to provide a correction function to resample the image with a constant magnification across the full field of view. The camera distortion tests were carried out in the JOP optical laboratory, at ambient conditions (P = 1013 hPa, T = 24 °C). Since the image plane position is adjusted for vacuum, and the test target distance was limited by the laboratory space, the test images were not perfectly in focus. This fact has a limiting effect on the accuracy of the distortion maps. In order to improve the image distortion correction, star-field images will be acquired during the cruise from Earth to Didymos. The ground tests were performed by three different targets:

- Black dots (10 mm diameter) on 20 mm pitch, self-illuminating cool white LED background
- Black and white chequerboard, 10 mm by 10 mm squares, ambient illumination from the laboratory lights
- Black and white chequerboard, 10 mm by 50 mm squares, ambient illumination from the laboratory lights

To improve the sharpness of the images, a circular aperture (20 mm diameter) was placed in front of the camera (Fig. 5).

Both cameras produced very similar distortion images. No apparent assembly effects (component tilt/decenter) were found. The ambient air pressure and the finite object distance resulted a strongly defocused image. Also, the illumination variation across the targets caused intensity variation on the images. These effects were strongly influencing the accuracy of the control points. The positional accuracy of the control points was estimated to be 1.5 pixel (min 0.9 pixel, maximum 5 pixel). As the first approximation of the distortion correction only radial distortion components were considered. The two cameras were supposed to behave similarly, so the radial distortion fit was calculated for a unified shift dataset.

The radial distortion is provided as a degree-3 polynomial function:

$$D_{rad} = K_0 + K_1 r + K_2 r^2 + K_3 r^3$$

where D_{rad} is the radial distortion in mm, $K_0 \ldots K_3$ are the polynomial coefficients (Table), and r the radial distance of the image point, measured from the geometrical centre of the image: [509.5, 509.5] pixels. The polynomial coefficients describing this radial distortion are provided in Table 4.

Note that the distortion will be better evaluated in flight through imaging of reference star fields. Preliminary analysis suggests that the distortion is minimal: maximum error = 0.81 pixel, average error = 0.33 pixel.

3.7 Point Spread Function

The point spread function (PSF) was not measured on the ground, but instead calculated from many images of star fields acquired in the first 6 months of cruise. On star field images the average PSF size is less than 2 pixels including the pointing instability. The Gauss fit S parameter is about 0.8 pixel (1.6 pixel diameter) which encircles 65% of the star flux.

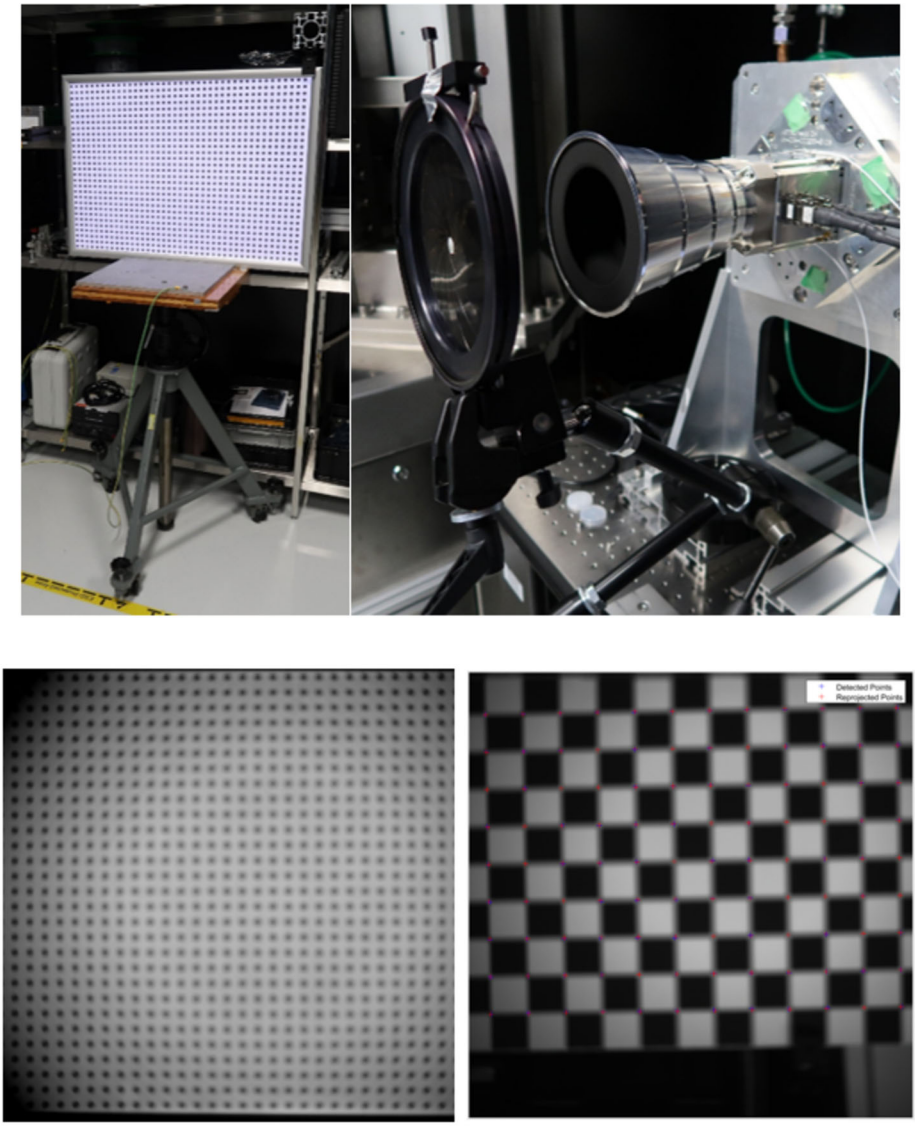

Fig. 5 Test setup for optical distortion measurements

Table 4 Polynomial coefficients for the radial distortion

K_0	K_1	K_2	K_3
0	-1.1398×10^{-4}	9.0621×10^{-5}	-1.3891×10^{-4}

3.8 Recommended Minimal Procedure for Image Calibration

The suggested minimal AFC flight calibration pipe should implement the following steps:

Table 5 Calibration targets

Target	RA	DEC
Starfield	07 h 21 m	−25d 34 m
Starfield	04 h 25 m	+15d 10 m
Vega	18 h 37 m	+38d 47 m
16 Cygni	19 h 42 m	+50d 31 m

1. Open image file(s): check data integrity, extract header metadata, extract binary content.
2. Convert image pixel 16-bit DNs to double precision numbers.
3. Remove bias based on the master bias frame.
4. Remove bad pixels.
5. Correct for dark current using the master dark image and the dark scaling equation with the header information (exposure time, detector temperature). Master dark images shall be updated during the mission.
6. Apply the flat field correction.
7. Correct linearity errors.
8. Scale the image to radiance or I/f (reflectance) units.
9. Apply distortion correction (if needed for accurate morphology or navigation)

3.9 In-Flight Calibration

To monitor the state of the instruments, we designed a set of calibration sequences to be acquired at regular intervals in flight. The sequences include monitoring of the dark and bias levels, observations of two reference star fields for measuring geometric distortions, and two standard stars for radiometric calibration. All targets are listed in Table 5. All observations will be acquired with multiple exposure times. These calibration activities will take place every 6 months during the cruise. After arrival at Didymos, we will monitor the dark and bias values on a weekly basis, and point to stars and star fields for radio/geo-metric calibration once per mission phase (see Sect. 4).

During cruise, Hera will have two unique opportunities to observe extended objects: the Earth/Moon system shortly after launch, and Mars/Deimos in March 2025.

The Earth/Moon images will be acquired at high phase angle ($> 75°$) a few days after launch. We expect the Earth to occupy at least 50 px, and the Moon at least 15 px in the AFC images, but the exact size depends on the spacecraft status after launch and how early the observations can be scheduled.

The Mars swing-by will allow for observations of a full rotation of Mars at varying scale, including many frame filling images. During the swing-by, Hera will cover a wide range of phase angles ($0° - 180°$), providing a excellent data set for radiometric calibration of the full detector. High-resolution images of well-known terrains will be used to refine our measurements of the geometric distortion. In addition, Hera's swing-by is timed so that Deimos will be in the field of view of the AFC, in between Hera and Mars, from a distance of 1000 km. This will allow to resolve a spatial scale of 95 m/px on the far side of Deimos (1.9 km/px on Mars in the same image). Figure 6 shows simulated views of the swing-by.

Although this article focuses on the AFC, it should be noted that we strive to acquire the best data for cross-calibration between all remote-sensing instruments on Hera (AFC, Hyperscout, TIRI). As much as possible, we align our calibration observations to target the same objects at the same time (stars, star fields, planets).

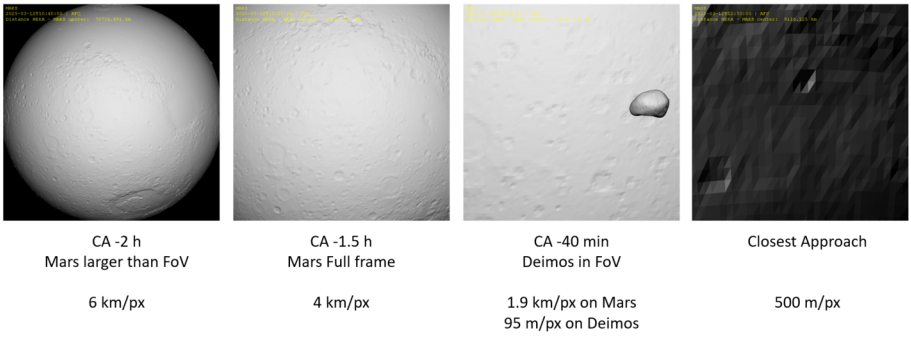

Fig. 6 Simulated AFC observations showing the expected views and pixel scale during the Mars swing-by. Exact time and distance of closest approach are preliminary, pending results of trajectory correction manoeuvres on the way to Mars. The simulation only shows the geometry of shape models, with a simple Lambert shading. This is not intended to be radiometrically correct. Simulations realized with the *shapeViewer* software, available at www.comet-toolbox.com

Table 6 Mission phases

Phase	Duration (weeks)	Distance (km)
ECP: Early Characterization Phase	6	30 - 20
PDP: Payload Deployment Phase	2	30 - 20
DCP: Detailed Characterization Phase	4	20 - 10
COP: Close Operations Phase	6	20 - 5
COP: EXperimental Phase	4	20 - 1

4 Asteroid Phase

The cruise phase activities are limited to commissioning and calibration activities, with the exception of the "farewell to Earth" images, and Deimos far side observations.

As we approach the asteroids, the AFC will perform a reconnaissance of the system with deep exposures to look for any eventual debris that could be hazardous to the mission. We will also acquire light curves to refine our understanding of the shape and spin properties of both asteroids.

The core AFC activities will take place at the Didymos system from December 2026 and last for at least 6 months. The mission is divided in 5 major phases (Table 6) which will bring Hera closer and closer to the asteroids, achieving full mapping of the two bodies at increasingly better resolution.

At the time of writing this article, the detailed trajectory of Hera in the Didymos system has only been fully evaluated until the end of DCP. We provide in Figs. 7 and 8 the planned distances, resolution, latitude and phase angle coverage in the first three phases in the mission. These shows that Hera will observe the full surface of both asteroids, except perhaps polar areas that may be permanently shadowed. The phase angle will be mostly between 40° and 60°, which provide ideal viewing conditions for mapping and shape reconstruction. In DCP, the trajectory provides 4 opportunities to observe the surface at zero phase from a distance of 10 km (i.e. 1 m/px resolution), which is intended to provide albedo measurements of both asteroids.

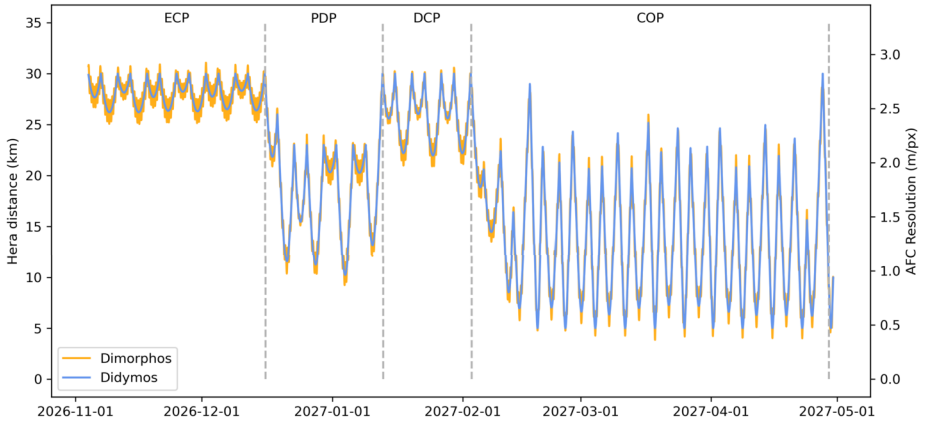

Fig. 7 Planned trajectory for the first four phases of the mission after arrival at Didymos, ECP: Early Characterization Phase, PDP: Payload Deployment Phase, DCP: Detailed Characterization Phase, COP: Close Operations Phase. All dates are preliminary and may change during cruise

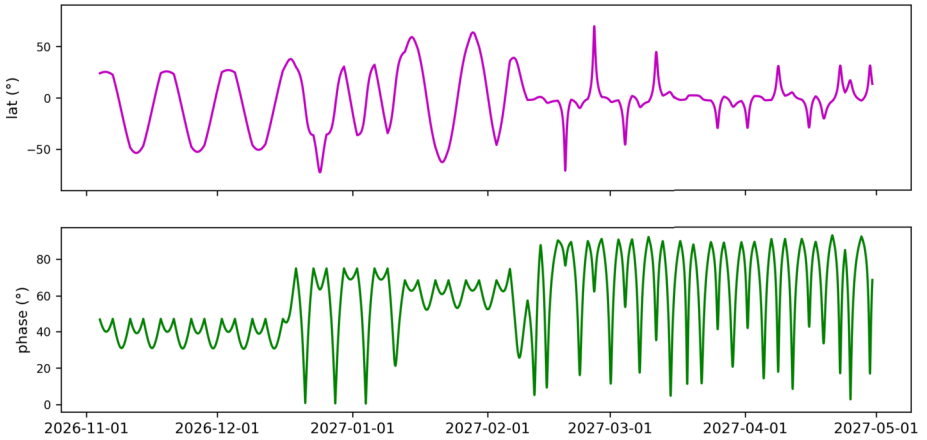

Fig. 8 Sub-spacecraft latitude and phase angle on Didymos/Dimorphos in the first four phases of the mission after arrival at Didymos. All dates are preliminary and may change during cruise

During the mission, the AFC mostly operates in a mapping mode. We want to ensure consistent data set with similar observations that repeat day after day in order to maximise the chance to detect changes, whether as surface transformation or dynamical evolution of the system. To achieve this, our baseline is to acquire one image every 10 min while in the Didymos system, with a duty cycle of 15 hours per day (+ 9 hours of downlink/manoeuvres). This ensures that Dimorphos will be observed for more than a full orbit every day (current orbital period 11.5 hours, Thomas et al. 2023). The mapping cadence may be reduced to 20 min at the end of the mission, when data volume might be more constrained.

This mapping data will be used for shape determination, orbital state, dynamics, morphological mapping, identification of DART crater and other features of interest, selection of fly-bys targets (in preparation of COP), change detection. Once per week, we plan some

deep exposures and fast cadence imaging to detect eventual dust emission or track potential debris in the system. These observations may be more frequent if needed.

Finally, we will make use of the synergy with other instruments to increase the science return of the mission. For instance:

- the AFC will track Dimorphos as it enters the shadow of Didymos to provide high-resolution context to the thermal imaging instrument (TIRI, Popescu et al. 2025). Similar joint observations will be acquired when tracking the shadow of Dimorphos cast onto Didymos.
- Global mappings of the asteroids with the Hyperscout instrument (Okada et al. 2025), at low phase angle, will allow to cross-calibrate our albedo measurements.
- At altitudes below 17 km, we will operate the AFC together with the laser altimeter PALT, in order to combine the ranging and imaging data to build better shape models of the asteroids.
- We will characterise the landing sites of Juventas and eventually Milani at high resolution, before and after landing, to better understand the response of the surface to the landing event.
- If the trajectory allows it, we plan to track the probes as they are released. Observing their landings as they occur might be challenging but possible if Hera is < 1 km from the cubesats.

Overall, the data to be acquired by the AFC amount to about 20,000 images, typically 90 exposures per day (135 MByte) in the asteroid phase.

5 Scientific Activities

ESA's Hera mission will bring the key measurements necessary to close the AIDA experiment: what is the actual momentum transferred by the impact (mass), what is the final state of Dimorphos? (crater, reshaped), what are the asteroids internal properties (rubble pile, monolith).

It is also a mission of many "firsts" for asteroid science, as detailed in Michel et al. (2022, 2025):

- First binary asteroid orbited by a space mission,
- Smallest asteroid ever visited by a space mission,
- First internal structure probing of a full asteroid,
- First asteroid visited near the disruption spin barrier.

These questions cannot be answered without the contributions from an instrument like the AFC, as imaging data is a necessary requisite for most of the studies carried out by the investigation team.

We have presented the technical specifications of the camera, and the calibration results, which gives confidence that the instrument is perfectly suited for its tasks. In parallel, the team has been developing many tools to analyse the data: from shape reconstruction pipelines (Preusker et al. 2017), to automated image processing for boulder statistics (Pajola et al. 2024) and morphology (Robin et al. 2024), roughness analysis (Vincent et al. 2023), as well as 3d visualisation software (Vincent 2018; Caballo-Perucha et al. 2024).

A key component of the science to be enabled by the AFC is the production of a shape model for each asteroid. This data product will be the reference for all studies that need to

Table 7 Requirements for stereo-photogrammetry

Parameter	Optimal	Minimal
Illumination variation	0°–10°	0°–10°
Stereo angle	10°–70°	15°–70°
Incidence angle	5°–65°	5°–85°
Emission angle	0°–65°	0°–65°
Sun phase angle	10°–170°	10°–170°

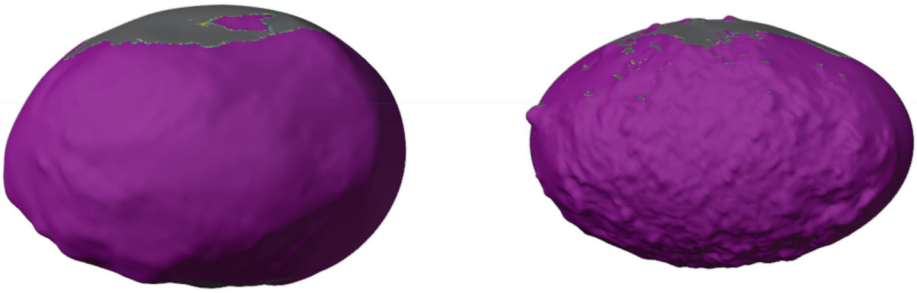

Fig. 9 Using our requirements, stereo coverage maps were calculated for Didymos (left) and Dimorphos (right) for the respective observation phases, whereby the number of images of a stereo constellation is marked in different colors. Here, we show the results for the optimal case in ECP. Green (three views), blue (four views), and purple colors (five and more views) indicate sufficient stereo conditions, whereas insufficient stereo conditions are marked with yellow and grey colors. Shape models oriented with North up, asteroids not to scale

know the volume of the asteroids (e.g. to derive density and porosity) and for morphological studies.

While images will be continuously acquired during the mission, and will be used for shape reconstruction, the first two phases of the mission (ECP: Early Characterization Phase, and DCP: Detailed Characterization Phase) are particularly well suited for stereo-photogrammetric analysis. In both phases we currently aim to acquire images with a 10 minutes cadence. To assess the expected quality of the shape reconstruction, we performed a study of the viewing conditions. Indeed, the stereo-photogrammetric analyses require a favourable image- and illumination geometry, because such geometry affects the quantity and quality of matched image points and resulting reconstructed surface points. Furthermore, the stereo constellation (stereo angle and number of stereo partners) influences the reconstruction result, where only a constellation with at least three stereo images results to a stable reconstruction of a surface point. Due to the rotational properties of both bodies the observation conditions vary during these observation phases, affecting the quality of stereo conditions accordingly. Table 7 defines two different parameter sets of stereo requirements which are intended to enable complete stereo coverage in gradations (Table 7).

Using the respective stereo requirements, stereo coverage maps were calculated for Didymos and Dimorphos for the respective observation phases (Fig. 9). Our simulations of the observing conditions show that the trajectory and attitude planned for ECP and DCP enable an excellent stereo coverage of all regions, on both asteroids, except for a few limited areas that may be permanently shadowed (Table 8). Although we recommend an imaging cadence of 10 min, a more relaxed cadence of 20 min, for 15 hours/day (accounting for downlink windows) appears sufficient to meet our goals.

Table 8 Summary of SPG feasability study. Surface area for which at least 5 stereo views meeting the "Minimal" or "Optimal" requirements will be obtained

Mission Phase	Didymos coverage	Dimorphos coverage
ECP	97.1% (minimal)	98.0% (minimal)
	81.3% (optimal)	80.3% (optimal)
DCP	98.6% (minimal)	93.5% (minimal)
	84.6% (optimal)	78.0% (optimal)

All the operations planning and analysis effort is coordinated by the instrument team, and the Hera Data Analysis Working Group (Michel et al. 2022), which ensure that the AFC data and derived high-level products will be available to the whole team in a timely manner.

6 Conclusion

At the time of writing this paper, Hera has successfully launched and is on its way to Didymos. Instruments are being commissioned, and the AFCs have been switched on. Images of the Earth and the Moon have been acquired for calibration purpose (Fig. 10), and show excellent behaviour from both cameras. A detailed calibration campaign will take place over the first 6 months of the mission, including the Mars swing-by. Results from this in-flight calibration will be presented in a future publication.

Beyond Planetary Defence, Hera provides a unique opportunity to observe in-situ a numerous but poorly known class of asteroids (binaries represent 15% of Near-Earth objects). The AFC data will be instrumental in assessing the dynamical state of the system and predict its long term evolution. As for surface properties, the DART mission has provided a first view of the system pre-impact (Barnouin et al. 2024) which covers, however, only a fraction of the surface of both asteroids (at 3.5 m/px for Didymos, and 35 cm/px for the global view of Dimorphos). While extremely useful, this data do not give us the complete picture, and we are missing global statistics on key morphological features such as craters and boulders, necessary to fully assess the age and evolution state of the surface. Global mapping with the AFC at multiple resolutions, will allow us to refine these statistics and build a complete picture, post-DART.

Indeed, it is a certainty that Dimorphos has changed because of the impact, and the AFC data will identify whether DART left a crater, or reshaped the body (Raducan et al. 2024). And if the latter, to what extent? nevertheless Didymos too may display significant changes as the result of ejected boulders re-impacting its surface. With a rotation period of only 2.25 h, the asteroid is very close to the theoretical disruption limit of a cohesion-less rubble pile (Agrusa et al. 2024). As evidenced by several studies (Barnouin et al. 2024; Bigot et al. 2024; Vincent et al. 2024), the equatorial region of Didymos is smoother, perhaps less cohesive, than other areas. It is likely that ejecta from Dimorphos may have fallen back on Didymos, and triggered landslides or mobilization of the surface. Such changes will be identifiable in AFC images, and the continuous mapping provided by the instrument will allow us to monitor the surface for any subsequent activity once Hera reaches Didymos.

The Hera mission will complete the AIDA experiment. By building a comprehensive characterisation of a Near-Earth Asteroids, Hera will give us the knowledge to defend against a potentially hazardous object, when the time comes. The Asteroid Framing Cameras, a core payload of the mission, have been thoroughly tested and calibrated before launch and are ready to support the mission in achieving its goals.

Fig. 10 First image acquired in space by AFC1 on 2024-10-11T21:25:06 UTC, showing the Earth (bottom left) and the Moon (centre) from a distance of approximately 1.6 million km. Earth is oriented with north pointing upwards, with the Pacific Ocean illuminated by the Sun

Acknowledgements The AFCs have been calibrated at the optical laboratory of Jena-Optronik GmbH (JOP). During the calibration tests the calibration process have been supervised by Hannah Goldberg (ESA) and Axel Kwiatkowski (JOP).

The calibration procedures were designed by Gábor Kovács and Balazs Vince Nagy (BME MOGI). The instruments have been supervised and operated by JOP engineers Axel Kwiatkowski and Karla Rossmann.

The calibration setups and the devices have been operated by MOGI.

Funding Information Open Access funding enabled and organized by Projekt DEAL. J.-B. V., P. M., G. K., B. V. N., and F. P. acknowledge support from ESA through contract 4000144275/24/NL/GLC

M.P. acknowledges support from the Italian Space Agency (ASI) through ASI-INAF Agreement No. 2022-8-HH.0.

Declarations

Competing Interests The authors declare no competing interests.

References

Agrusa HF, Zhang Y, Richardson DC, Pravec P, Ćuk M, Michel P, Ballouz R-L, Jacobson SA, Scheeres DJ, Walsh K, Barnouin O, Daly RT, Palmer E, Pajola M, Lucchetti A, Tusberti F, DeMartini JV, Ferrari F, Meyer AJ, Raducan SD, Sánchez P (2024) Direct n-body simulations of satellite formation around small asteroids: insights from dart's encounter with the Didymos system. Planet Sci J 5(2):54. https://doi.org/10.3847/PSJ/ad206b

Barnouin O, Ballouz R-L, Marchi S, Vincent J-B, Agrusa H, Zhang Y, Ernst CM, Pajola M, Tusberti F, Lucchetti A, Daly RT, Palmer E, Walsh KJ, Michel P, Sunshine JM, Rizos JL, Farnham TL, Richardson DC, Parro LM, Murdoch N, Robin CQ, Hirabayashi M, Kahout T, Asphaug E, Raducan SD, Jutzi M, Ferrari F, Hasselmann PHA, CampoBagatin A, Chabot NL, Li J-Y, Cheng AF, Nolan MC, Stickle AM, Karatekin O, Dotto E, Della Corte V, Mazzotta Epifani E, Rossi A, Gai I, Deshapriya JDP, Bertini I, Zinzi A, Trigo-Rodriguez JM, Beccarelli J, Ivanovski SL, Brucato JR, Poggiali G, Zanotti G, Amoroso M, Capannolo A, Cremonese G, Dall'Ora M, Ieva S, Impresario G, Lavagn M, Modenini D, Palumbo P, Perna D, Pirrotta S, Tortora P, Zannoni M, Rivkin AS (2024) The geology and evolution of the near-Earth binary asteroid system (65803) Didymos. Nat Commun 15(1):6202. https://doi.org/10.1038/s41467-024-50146-x

Bigot J, Lombardo P, Murdoch N, Scheeres DJ, Vivet D, Zhang Y, Sunshine J, Vincent JB, Barnouin OS, Ernst CM, Daly RT, Sunday C, Michel P, Campo-Bagatin A, Lucchetti A, Pajola M, Rivkin AS, Chabot NL (2024) The bearing capacity of asteroid (65803) Didymos estimated from boulder tracks. Nat Commun 15:6204. https://doi.org/10.1038/s41467-024-50149-8

Caballo-Perucha P, Nowak R, Steinlechner H, Paar G, Traxler C, Vincent J (2024) PRo3D-GIS tool for Hera: visualization and analysis of two use cases. In: Europlanet Science Congress. EPSC2024-322. https://doi.org/10.5194/epsc2024-322

Cheng AF, Rivkin AS, Michel P, Atchison J, Barnouin O, Benner L, Chabot NL, Ernst C, Fahnestock EG, Kueppers M, Pravec P, Rainey E, Richardson DC, Stickle AM, Thomas C (2018) AIDA DART asteroid deflection test: planetary defense and science objectives. Planet Space Sci 157:104–115. https://doi.org/10.1016/j.pss.2018.02.015

Cheng AF, Agrusa HF, Barbee BW, Meyer AJ, Farnham TL, Raducan SD, Richardson DC, Dotto E, Zinzi A, Della Corte V, Statler TS, Chesley S, Naidu SP, Hirabayashi M, Li J-Y, Eggl S, Barnouin OS, Chabot NL, Chocron S, Collins GS, Daly RT, Davison TM, DeCoster ME, Ernst CM, Ferrari F, Graninger DM, Jacobson SA, Jutzi M, Kumamoto KM, Luther R, Lyzhoft JR, Michel P, Murdoch N, Nakano R, Palmer E, Rivkin AS, Scheeres DJ, Stickle AM, Sunshine JM, Trigo-Rodriguez JM, Vincent J-B, Walker JD, Wünnemann K, Zhang Y, Amoroso M, Bertini I, Brucato JR, Capannolo A, Cremonese G, Dall'Ora M, Deshapriya PJD, Gai I, Hasselmann PH, Ieva S, Impresario G, Ivanovski SL, Lavagna M, Lucchetti A, Epifani EM, Modenini D, Pajola M, Palumbo P, Perna D, Pirrotta S, Poggiali G, Rossi A, Tortora P, Zannoni M, Zanotti G (2023) Momentum transfer from the DART mission kinetic impact on asteroid Dimorphos. Nature 616(7957):457–460. https://doi.org/10.1038/s41586-023-05878-z. arXiv:2303.03464 [astro-ph.EP]

Daly RT, Ernst CM, Barnouin OS, Chabot NL, Rivkin AS, Cheng AF, Adams EY, Agrusa HF, Abel ED, Alford AL, Asphaug EI, Atchison JA, Badger AR, Baki P, Ballouz R-L, Bekker DL, Bellerose J, Bhaskaran S, Buratti BJ, Cambioni S, Chen MH, Chesley SR, Chiu G, Collins GS, Cox MW, DeCoster ME, Ericksen PS, Espiritu RC, Faber AS, Farnham TL, Ferrari F, Fletcher ZJ, Gaskell RW, Graninger DM, Haque MA, Harrington-Duff PA, Hefter S, Herreros I, Hirabayashi M, Huang PM, Hsieh S-YW, Jacobson SA, Jenkins SN, Jensenius MA, John JW, Jutzi M, Kohout T, Krueger TO, Laipert FE, Lopez NR, Luther R, Lucchetti A, Mages DM, Marchi S, Martin AC, McQuaide ME, Michel P, Moskovitz NA, Murphy IW, Murdoch N, Naidu SP, Nair H, Nolan MC, Ormö J, Pajola M, Palmer EE, Peachey JM, Pravec P, Raducan SD, Ramesh KT, Ramirez JR, Reynolds EL, Richman JE, Robin CQ, Rodriguez LM, Roufberg LM, Rush BP, Sawyer CA, Scheeres DJ, Scheirich P, Schwartz SR, Shannon MP, Shapiro BN, Shearer CE, Smith EJ, Steele RJ, Steckloff JK, Stickle AM, Sunshine JM, Superfin EA, Tarzi ZB,

Thomas CA, Thomas JR, Trigo-Rodríguez JM, Tropf BT, Vaughan AT, Velez D, Waller CD, Wilson DS, Wortman KA, Zhang Y (2023) Successful kinetic impact into an asteroid for planetary defence. Nature 616(7957):443–447. https://doi.org/10.1038/s41586-023-05810-5. arXiv:2303.02248 [astro-ph.EP]

Kovács G, Nathues A, Sierks H, Gutiérrez Marqués P, Hoffmann M, Thangjam GS (2024) The scientific calibration of the Dawn Framing Camera. Space Sci Rev 220(1):4. https://doi.org/10.1007/s11214-023-01039-w

Michel P, Küppers M, Bagatin AC, Carry B, Charnoz S, de Leon J, Fitzsimmons A, Gordo P, Green SF, Hérique A, Juzi M, Karatekin Ö, Kohout T, Lazzarin M, Murdoch N, Okada T, Palomba E, Pravec P, Snodgrass C, Tortora P, Tsiganis K, Ulamec S, Vincent J-B, Wünnemann K, Zhang Y, Raducan SD, Dotto E, Chabot N, Cheng AF, Rivkin A, Barnouin O, Ernst C, Stickle A, Richardson DC, Thomas C, Arakawa M, Miyamoto H, Nakamura A, Sugita S, Yoshikawa M, Abell P, Asphaug E, Ballouz R-L, Bottke WF, Lauretta DS, Walsh KJ, Martino P, Carnelli I (2022) The ESA Hera Mission: detailed characterization of the DART impact outcome and of the binary asteroid (65803) Didymos. Planet Sci J 3(7):160. https://doi.org/10.3847/PSJ/ac6f52

Michel P, Küppers M, Fitzsimmons A et al (2025) The Hera space mission in the context of small near-Earth asteroid missions in the past, present and future. Space Sci Rev 221:70. https://doi.org/10.1007/s11214-025-01195-1

Okada T, Tanaka S, Sakatani N et al (2025) The Thermal InfraRed Imager on Hera. Space Sci Rev 221:104. https://doi.org/10.1007/s11214-025-01227-w

Pajola M, Tusberti F, Lucchetti A, Barnouin O, Cambioni S, Ernst CM, Dotto E, Daly RT, Poggiali G, Hirabayashi M, Nakano R, Epifani EM, Chabot NL, Della Corte V, Rivkin A, Agrusa H, Zhang Y, Penasa L, Ballouz R-L, Ivanovski S, Murdoch N, Rossi A, Robin C, Ieva S, Vincent JB, Ferrari F, Raducan SD, Campo-Bagatin A, Parro L, Benavidez P, Tancredi G, Karatekin Ö, Trigo-Rodriguez JM, Sunshine J, Farnham T, Asphaug E, Deshapriya JDP, Hasselmann PHA, Beccarelli J, Schwartz SR, Abell P, Michel P, Cheng A, Brucato JR, Zinzi A, Amoroso M, Pirrotta S, Impresario G, Bertini I, Capannolo A, Caporali S, Ceresoli M, Cremonese G, Dall'Ora M, Gai I, Casajus LG, Gramigna E, Manghi RL, Lavagna M, Lombardo M, Modenini D, Palumbo P, Perna D, Tortora P, Zannoni M, Zanotti G (2024) Evidence for multi-fragmentation and mass shedding of boulders on rubble-pile binary asteroid system (65803) Didymos. Nat Commun 15:6205. https://doi.org/10.1038/s41467-024-50148-9

Popescu MM, de León J, Prodan GP et al (2025) HyperScout-H: the hyperspectral imager for the ESA Hera mission. Space Sci Rev 221:112. https://doi.org/10.1007/s11214-025-01237-8

Preusker F, Scholten F, Matz K-D, Roatsch T, Hviid SF, Mottola S, Knollenberg J, Kührt E, Pajola M, Oklay N, Vincent J-B, Davidsson B, A'Hearn MF, Agarwal J, Barbieri C, Barucci MA, Bertaux J-L, Bertini I, Cremonese G, Da Deppo V, Debei S, De Cecco M, Fornasier S, Fulle M, Groussin O, Gutiérrez PJ, Güttler C, Ip W-H, Jorda L, Keller HU, Koschny D, Kramm JR, Küppers M, Lamy P, Lara LM, Lazzarin M, Lopez Moreno JJ, Marzari F, Massironi M, Naletto G, Rickman H, Rodrigo R, Sierks H, Thomas N, Tubiana C (2017) The global meter-level shape model of comet 67P/Churyumov-Gerasimenko. Astron Astrophys 607:1. https://doi.org/10.1051/0004-6361/201731798

Raducan SD, Jutzi M, Cheng AF, Zhang Y, Barnouin O, Collins GS, Daly RT, Davison TM, Ernst CM, Farnham TL, Ferrari F, Hirabayashi M, Kumamoto KM, Michel P, Murdoch N, Nakano R, Pajola M, Rossi A, Agrusa HF, Barbee BW, Syal MB, Chabot NL, Dotto E, Fahnestock EG, Hasselmann PH, Herreros I, Ivanovski S, Li J-Y, Lucchetti A, Luther R, Ormö J, Owen M, Pravec P, Rivkin AS, Robin CQ, Sánchez P, Tusberti F, Wünnemann K, Zinzi A, Epifani EM, Manzoni C, May BH (2024) Physical properties of asteroid Dimorphos as derived from the DART impact. Nat Astron 8:445–455. https://doi.org/10.1038/s41550-024-02200-3. arXiv:2403.00667 [astro-ph.EP]

Robin CQ, Duchene A, Murdoch N, Vincent J-B, Lucchetti A, Pajola M, Ernst CM, Daly RT, Barnouin OS, Raducan SD, Michel P, Hirabayashi M, Stott A, Cuervo G, Jawin ER, Trigo-Rodriguez JM, Parro LM, Sunday C, Vivet D, Mimoun D, Rivkin AS, Chabot NL (2024) Mechanical properties of rubble pile asteroids (Dimorphos, Itokawa, Ryugu, and Bennu) through surface boulder morphological analysis. Nat Commun 15:6203. https://doi.org/10.1038/s41467-024-50147-w

Thomas CA, Naidu SP, Scheirich P, Moskovitz NA, Pravec P, Chesley SR, Rivkin AS, Osip DJ, Lister TA, Benner LAM, Brozović M, Contreras C, Morrell N, RoŽek A, Kušnirák P, Hornoch K, Mages D, Taylor PA, Seymour AD, Snodgrass C, Jørgensen UG, Dominik M, Skiff B, Polakis T, Knight MM, Farnham TL, Giorgini JD, Rush B, Bellerose J, Salas P, Armentrout WP, Watts G, Busch MW, Chatelain J, Gomez E, Greenstreet S, Phillips L, Bonavita M, Burgdorf MJ, Khalouei E, Longa-Peña P, Rabus M, Sajadian S, Chabot NL, Cheng AF, Ryan WH, Ryan EV, Holt CE, Agrusa HF (2023) Orbital period change of Dimorphos due to the DART kinetic impact. Nature 616(7957):448–451. https://doi.org/10.1038/s41586-023-05805-2. arXiv:2303.02077 [astro-ph.EP]

Vincent J-B (2018) shapeViewer, a mapping tool for the morphological analysis of small bodies and mission operations planning. In: 49th Annual Lunar and Planetary Science Conference. Lunar and Planetary Science Conference, p 1281

Vincent J-B, Barnouin O, Ernst C, Hasselmann PH, Ieva S, Lucchetti A, Michel P, Murdoch N, Pajola M, Sunshine J, Zinzi A (2023) Macro-scale roughness and morphological units on Didymos and Dimorphos. In: Asteroids, comets, meteors conference. LPI contributions, vol 2851, p 2259

Vincent J-B, Asphaug E, Barnouin O, Beccarelli J, Benavidez PG, Campo-Bagatin A, Chabot NL, Ernst CM, Hasselmann PH, Hirabayashi M, Ieva S, Karatekin Kašpárek T, Kohout T, Lin Z-Y, Lucchetti A, Michel P, Murdoch N, Pajola M, Parro LM, Raducan SD, Sunshine J, Tancredi G, Trigo-Rodriguez JM, Zinzi A (2024) Macroscale roughness reveals the complex history of asteroids Didymos and Dimorphos. Planet Sci J 5(10):236. https://doi.org/10.3847/PSJ/ad7a01

Authors and Affiliations

Jean-Baptiste Vincent[1] · Gábor Kovács[2] · Balázs V. Nagy[2] · Frank Preusker[1] · Naomi Murdoch[3] · Maurizio Pajola[4] · Michael Kueppers[5] · Patrick Michel[6,7] · Seiji Sugita[7] · Hannah Goldberg[8]

✉ J.-B. Vincent
jean-baptiste.vincent@dlr.de

1 DLR Institute of Planetary Research, Berlin, Germany

2 Department of Mechatronics, Optics and Engineering Informatics, Budapest University of Technology and Economics, Budapest, Hungary

3 Institut Supérieur de l'Aéronautique et de l'Espace (ISAE-SUPAERO), Université de Toulouse, Toulouse, France

4 Astronomical Observatory of Padova, INAF, Padova, Italy

5 European Space Astronomy Centre, European Space Agency, Villanueva de la Cañada, Madrid, Spain

6 Observatoire de la Côte d'Azur, CNRS, Laboratoire Lagrange, Université Côte d'Azur, Nice, France

7 Department of Systems Innovation, School of Engineering, The University of Tokyo, Tokyo, Japan

8 Space Science Laboratory, University of California, Berkeley Berkeley, USA